RESEARCH ARTICLE

Check for updates

Noncovalent induced circular dichroism sensors based on a chiral metal–organic framework: chiral induction synthesis, quantitative enantioselective sensing and noncovalent sensing mechanism†

Yanyu Zhu, Tianyang Ding, Xu Zhang, Yanan Zhou, Jiahui Yu, Xin Li, Hanwen Zheng, Zhengang Sun ⓘ * and Chengqi Jiao*

As an important class of chiral optical sensors, chiral induced circular dichroism (ICD) sensors have received increasing attention. Herein, a series of monometallic and bimetallic centered metal–organic frameworks (MOFs) with the same crystal structure, namely [Cu(L)(2,2′-bipy)]·H$_2$O (**LNNU-2**), [Cd(L)(2,2′-bipy)(H$_2$O)] (**LNNU-3**) and [Zn$_x$Cu$_y$(L)(2,2′-bipy)]·H$_2$O (x : y = 9.6 : 0.4–1.0 : 9.0) (H$_2$L = HOOCC$_6$H$_4$CH$_2$PO(OH)(OC$_2$H$_5$), 2,2′-bipy = 2,2′-bipyridine), have been successfully synthesized for studying the noncovalent ICD sensing mechanism. **LNNU-2** shows excellent ICD sensing performance due to the strong metal coordination interaction between **LNNU-2** and chiral tryptophan (Trp). In contrast, there is no ICD effect between **LNNU-3** and chiral Trp due to the absence of metal coordination interaction. The results indicate that the metal coordination interaction plays a decisive role in generating and amplifying ICD signals in this sensing system. Compared to the previously reported **LNNU-1** ([Zn(L)(2,2′-bipy)]·H$_2$O) sensor, **LNNU-2** is not only capable of quantifying the enantiomeric composition of chiral Trp samples at a lower concentration but also enables highly selective and accurate determination of L-Trp concentration in water, mixed natural amino acids and simulated blood plasma components by the circular dichroism (CD) titration method. **LNNU-2** also allows the accurate determination of the absolute configuration and enantiomeric excess (ee) values of two chiral aromatic amino alcohols in pure water. Additionally, the effects of different chiral amino acids as chiral inducers on the chiral induction synthesis of enantio-enriched **LNNU-2** were investigated. As a result, the enantioenriched (*P*)-**LNNU-2** and (*M*)-**LNNU-2** were successfully obtained using L-alanine (L-Ala) and D-alanine (D-Ala) as chiral inducers, respectively.

Introduction

Chirality is fundamental in nature and vital in chemistry, biology, life sciences, materials sciences, and other fields.[1–7] The enantiomers of chiral molecules often exhibit different pharmacological, metabolic, therapeutic or toxicological properties, but have the same physical and chemical properties in an achiral environment.[8,9] Therefore, the rapid, highly selective and accurate determination of the enantiomeric composition of chiral analytes is extremely important. Over the past decades, the most commonly applied techniques have been

School of Chemistry and Chemical Engineering, Liaoning Normal University, Dalian 116029, China. E-mail: szg188@163.com, jiaochengqi1989@163.com

†Electronic supplementary information (ESI) available: Experimental details, crystallographic details, PXRD, FT-IR and CD spectra, thermal analysis, the results of ICP measurements and L-Trp concentration determination. CCDC 1964191, 1964192 and 1964196. For ESI and crystallographic data in CIF or other electronic format see DOI: https://doi.org/10.1039/d3qi00251a

chromatography with chiral stationary phases and nuclear magnetic resonance (NMR) analysis with chiral solvating or derivatizing agents.[10–15] However, these methods are not suitable for rapid analysis, due to expensive instrumentation, time-consuming steps, and sophisticated programs. In contrast, chiral optical sensing is considered to be a promising method due to the advantages of simple operation, rapid response, high sensitivity and low cost.[16–25] Chiral optical sensing can allow the enantioselective recognition of chiral molecules by monitoring changes in the fluorescence/circular dichroism (CD) signals of chiral optical sensors. Thus, the rational design and construction of chiral optical sensors is of great importance for the determination of the enantiomeric composition of chiral analytes.

In recent years, chiral metal–organic frameworks (MOFs) have become an important class of chiral optical sensing materials due to their stable chiral structures, designable functional sites and specific porosity.[26–39] Some optical sensors based on chiral MOFs have been reported for the enantio-

2818 | *Inorg. Chem. Front.*, 2023, **10**, 2818–2828

This journal is © the Partner Organisations 2023

selective sensing of amino acids, amino alcohols, drugs, *etc.*[26–34] Despite the considerable progress in the design and application of optical sensors based on chiral MOFs, several challenges remain: (1) relying on a single optical signal change to achieve differentiation of target enantiomers, which is susceptible to interference from external factors and has poor resistance to background interference; (2) reports on the accurate determination of enantiomeric excess (ee) values for chiral analytes are rare. It is worth noting that the induced circular dichroism (ICD) technique may provide a feasible strategy for dealing with the above problems. Strong ICD signals could be generated through covalent or noncovalent interactions between the sensor and the chiral analyte.[19,40–51] The generation of red-shifted ICD signals (above 300 nm) is likely to eliminate the interference from chiral impurities when quantitative analysis of ee values is performed. Recently, a reusable, highly selective and sensitive ICD sensor (**LNNU-1**) based on a chiral MOF was first reported by our group.[51] This ICD sensor could accurately determine the absolute configuration and enantiomeric ratio of chiral tryptophan (Trp) in water, mixed natural amino acids, and simulated blood plasma components, respectively. However, there are three unresolved problems: (1) although it has been confirmed that the ICD effect between **LNNU-1** and chiral Trp is due to three simultaneous noncovalent interactions (metal coordination, hydrogen bonding and $\pi \cdots \pi$ interactions) in aqueous solution (Fig. S1†), it is necessary to further explore the effect of these noncovalent interactions on the generation and amplification of ICD signals; (2) **LNNU-1** was unable to determine the concentration of chiral Trp in water or mixed chiral amino acids when using the CD titration method; (3) **LNNU-1** was not capable of quantifying the enantiomeric composition of other chiral compounds by noncovalent ICD sensing. Among the above problems, the study of the noncovalent ICD sensing mechanism is very pivotal. It may provide a strategy for the targeted design and synthesis of highly sensitive ICD sensors based on chiral MOFs. Highly sensitive ICD sensors have the potential to determine the concentration of chiral Trp in water or mixed chiral amino acids, and to analyze the enantiomeric composition of other chiral compounds. Previous work has demonstrated that the $\pi \cdots \pi$ interaction is an indispensable noncovalent interaction for the ICD sensing of chiral aromatic amino acids (L-/D-Trp).[51] Herein, only metal coordination and hydrogen bonding interactions in this ICD sensing system should be further investigated. Our idea is to synthesize new chiral MOFs that should be isomorphic to **LNNU-1** but have other unsaturated or saturated metal centers. By observing the differences in the ICD signals between these MOFs and chiral Trp/chiral Trp derivatives, it is possible to determine the effects of metal coordination and hydrogen bonding interactions on the generation and amplification of ICD signals.

Thus, a series of monometallic and bimetalliccentered MOFs with the same crystal structure, namely [Cu(L)(2,2′-bipy)]·H$_2$O (**LNNU-2**), [Cd(L)(2,2′-bipy)(H$_2$O)] (**LNNU-3**) and [Zn$_x$Cu$_y$(L)(2,2′-bipy)]·H$_2$O $(x:y = 9.6:0.4–1.0:9.0)$ (H$_2$L = HOOCC$_6$H$_4$CH$_2$PO(OH)(OC$_2$H$_5$), 2,2′-bipy = 2,2′-bipyridine),
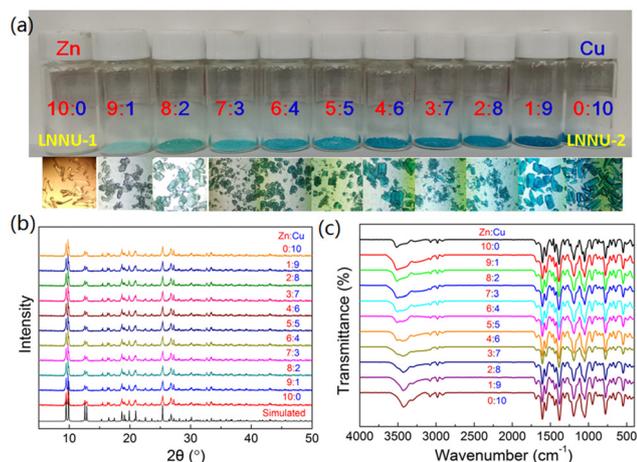
have been successfully synthesized. It is found that the metal coordination interaction is critical and indispensable to this ICD sensing system. The strength of ICD signals increased with the enhancement of Lewis acidity in the metal center of the above MOFs. Subsequently, **LNNU-2** interacted with L-Trp and three L-Trp derivatives containing different active sites, resulting in different ICD effects. These results further confirmed that the metal coordination interaction played a decisive role in the generation of ICD signals, while the hydrogen bonding interaction only affected the amplification degree of the ICD signal. Compared with **LNNU-1**, **LNNU-2** has a higher sensitivity for ICD sensing of chiral Trp. It allows the highly selective and accurate determination of L-Trp concentration in water, mixed natural amino acids and simulated blood plasma components by the CD titration method. Moreover, **LNNU-2** achieves the accurate determination of the absolute configuration and ee values of two chiral aromatic amino alcohols in water without the involvement of any organic solvent. Inspired by the results of the noncovalent ICD sensing mechanism, we investigated the effects of different chiral amino acids as chiral inducers on the chiral induction synthesis of enantioenriched **LNNU-2**. Surprisingly, the enantioenriched (*P*)-**LNNU-2** and (*M*)-**LNNU-2** were successfully obtained using L-alanine (L-Ala) and D-alanine (D-Ala) as chiral inducers, respectively.

Results and discussion

Synthesis, characterization and stability

A new chiral MOF, [Cu(L)(2,2′-bipy)]·H$_2$O (**LNNU-2**), was successfully synthesized by selecting the copper^{II} (Cu^{II}) ion with stronger Lewis acidity to replace the zinc^{II} (Zn^{II}) ion of **LNNU-1**. **LNNU-2** was isomorphic to **LNNU-1**, and the crystal structure and characterization of **LNNU-2** are provided in the ESI (Tables S1 and S2 and Fig. S2†). In addition, a series of Zn^{II} and Cu^{II} ion co-doped bimetallic MOFs isomorphic to **LNNU-1**, [Zn$_x$Cu$_y$(L)(2,2′-bipy)]·H$_2$O $(x:y = 9.6:0.4–1.0:9.0)$, were also successfully obtained. All the above products were block crystals, and the color of these crystals gradually deepened with the increase in the amount of Cu^{II} ions (Fig. 1a). The powder X-ray diffraction (PXRD) patterns and Fourier transform infrared (FT–IR) spectra showed that the above bimetallic MOFs have the same crystal structure as **LNNU-1** (Fig. 1b and c). Additionally, the actual molar ratios of Zn^{II}/Cu^{II} ions in the bimetallic MOFs were detected using an inductively coupled plasma emission spectrometer (ICP). As shown in Table S3,† the content of Cu^{II} ions in the products of bimetallic MOFs increased with the increase of the amount of the raw material Cu(CH$_3$COO)$_2$·H$_2$O, while the content of Zn^{II} ions decreased with the decrease of the amount of raw material Zn(CH$_3$COO)$_2$·2H$_2$O.

Subsequently, the stabilities of **LNNU-2** and a series of bimetallic MOFs were investigated. **LNNU-2** and bimetallic MOFs have similar thermal gravimetric (TG) curves, and thus, **LNNU-2** was used as a representative (Fig. S3a and b†). Thermal gravimetric and differential thermal analysis

This journal is © the Partner Organisations 2023

Inorg. Chem. Front., 2023, **10**, 2818–2828 | **2819**

Fig. 1 (a) The images, (b) PXRD patterns and (c) FT–IR spectra of **LNNU-1**, **LNNU-2** and the bimetallic MOFs.

Fig. 2 (a) CD spectra of the suspensions of **LNNU-1**@L-Trp, **LNNU-2**@L-Trp and a series of bimetallic MOFs@L-Trp; (b) CD spectra of the suspensions of **LNNU-1**@D/L-Trp, **LNNU-2**@D/L-Trp and **LNNU-3**@D/L-Trp; (c) CD spectra of aqueous solutions of L-Trp and its derivatives, and the suspensions of **LNNU-2**@L-Trp, **LNNU-2**@L-TrpNH$_2$, **LNNU-2**@L-TrpOMe and **LNNU-2**@NAc-L-Trp.

(TG–DTA), PXRD patterns and FT–IR spectra of **LNNU-2** showed that its framework structure could be stable up to 200 °C (Fig. S3a, c and d†). In addition, the PXRD patterns and FT–IR spectra of **LNNU-2** after immersing in pure water and the aqueous solution of L-Trp (2.5×10^{-3} M) indicated that the framework structure of **LNNU-2** remained stable (Fig. S4†). The above results indicated that **LNNU-2** and a series of Zn^{II} and Cu^{II} ion co-doped bimetallic MOFs were successfully obtained, and they could be used to study the noncovalent ICD sensing mechanism.

The noncovalent ICD sensing mechanism

The suspensions of **LNNU-1**@L-Trp, **LNNU-2**@L-Trp and a series of bimetallic MOFs@L-Trp were analyzed by CD spectroscopy under identical conditions. As expected, the ICD signal intensities of the above suspensions increased with the increasing content of Cu^{II} ions in the MOFs, and the ICD signals were gradually red-shifted (Fig. 2a and Table S4†). In particular, the complete replacement of Zn^{II} ions with Cu^{II} ions caused a dramatic increase in the measured intensity. The crystal structures of the above MOFs were identical, and thus, the variation in the ICD signal could be mainly attributed to the different Lewis acidities of the metal centers in the MOFs. Since the Lewis acidity of the Cu^{II} ion was stronger than that of the Zn^{II} ion, it was more likely to interact with the nitrogen (N) atom of the amino group in Trp. This resulted in an amplification of the ICD signal. Then, if the coordination geometry of the metal center of the MOF is saturated, could it produce the ICD effect after interacting with chiral Trp? Inspired by the above idea, we tried to synthesize a new MOF with the saturated coordination mode of the metal center by replacing the Zn^{II} ion with the cadmium^{II} (Cd^{II}) ion having the same d^{10} electron configuration to self-assemble with H$_2$L and 2,2′-bipy. Fortunately, a new chiral MOF, [Cd(L)(2,2′-bipy)(H$_2$O)] (**LNNU-3**), was successfully synthesized. Single-crystal structural analysis indicated that a lattice water molecule (O1
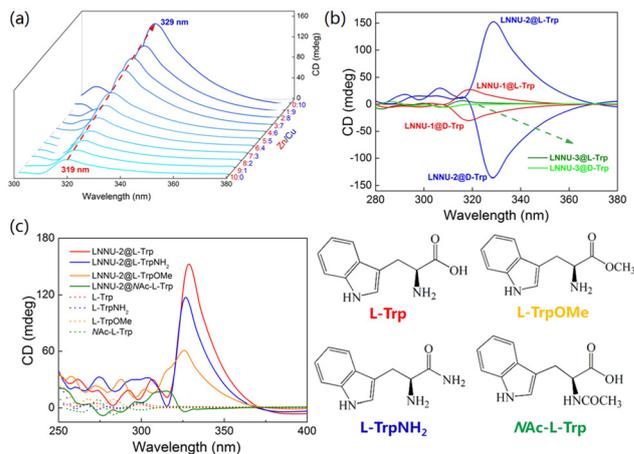
W) in the crystal structure of **LNNU-1** became a coordination water molecule (O6) in **LNNU-3** (Fig. S5 and Tables S5, S6†). Thus, the metal center of **LNNU-3** adopted a saturated coordination mode, while the framework of **LNNU-3** was basically the same as that of **LNNU-1**. The chiral characterization and stability of **LNNU-3** are provided in the ESI (Fig. S6†). Then, the suspensions of **LNNU-1**@D/L-Trp, **LNNU-2**@D/L-Trp and **LNNU-3**@D/L-Trp were analyzed by CD spectroscopy under the same conditions (Fig. 2b). The results showed that the suspensions of **LNNU-3**@D/L-Trp did not produce an ICD signal due to the absence of the unsaturated coordination metal center. In contrast, the suspensions of both **LNNU-1**@D/L-Trp and **LNNU-2**@D/L-Trp produced obvious enantiomeric ICD signals. The above results indicated that the metal coordination interaction was critical and indispensable in this sensing system. The strength of the ICD signal increased with the enhancement of the Lewis acidity of the metal center of the MOFs.

To further explore the effects of metal coordination and hydrogen bonding interactions on the generation and amplification of ICD signals, L-Trp and three L-Trp derivatives with different active sites were selected to interact with **LNNU-2**, respectively. As shown in Fig. 2c and Table S7,† the ICD signal intensity of the **LNNU-2**@analyte suspension followed the order **LNNU-2**@L-Trp > **LNNU-2**@L-TrpNH$_2$ > **LNNU-2**@L-TrpOMe > **LNNU-2**@NAc-L-Trp. This result showed that the ICD signal intensity of the **LNNU-2**@L-Trp suspension was the strongest, indicating that multiple noncovalent interactions facilitated the output and amplification of the ICD signal. L-TrpNH$_2$ could be regarded as a molecule formed by replacing the –COOH in L-Trp with –CONH$_2$. Although –CONH$_2$ could also participate in the formation of hydrogen bonding, the hydrogen bonding strength of N–H···O is weaker than that of O–H···O. Therefore, the ICD signal intensity of the **LNNU-2**@L-

2820 | *Inorg. Chem. Front.*, 2023, **10**, 2818–2828

This journal is © the Partner Organisations 2023

TrpNH$_2$ suspension was slightly weaker than that of **LNNU-2**@L-Trp suspension. The main difference between L-TrpOMe and L-Trp was the substitution of –COOH by –COOCH$_3$, resulting in no hydrogen bonding interaction between L-TrpOMe and **LNNU-2**. Therefore, the ICD signal intensity of the **LNNU-2**@L-TrpOMe suspension was significantly weaker than that of **LNNU-2**@L-Trp and **LNNU-2**@L-TrpNH$_2$ suspensions. In contrast, when –NHCOCH$_3$ completely replaced –NH$_2$ in L-Trp, the metal coordination interaction disappeared in the sensing system, resulting in no ICD signal output in the **LNNU-2**@NAc-L-Trp suspension. The above results suggested that the metal coordination interaction played a decisive role in the generation of ICD signals, and the hydrogen bonding interaction only affected the amplifiication degree of the ICD signal.

Determination of L-Trp concentration

L-Trp is an essential amino acid that is very important for humans and animals, and its imbalance or deficiency may lead to several chronic diseases.[52,53] Although **LNNU-1** exhibited good enantioselective sensing of chiral Trp at a millimolar analytical concentration in the previous research,[51] it was unable to detect the concentration of L-Trp based on the ICD response (Fig. S7†). As demonstrated in Fig. 2b and Table S4,† the ICD signal intensity of the **LNNU-2**@L-Trp suspension was about 5.8 times higher than that of the **LNNU-1**@L-Trp suspension. Therefore, **LNNU-2** should have a higher sensitivity for ICD sensing of L-Trp. This result provided a possibility for achieving the accurate determination of L-Trp concentration in water using the CD titration method.

Subsequently, the CD spectra of the **LNNU-2** suspension (2.0 mg **LNNU-2** in 2.0 mL deionized water after treating by ultrasonication for 20 minutes) were measured *in situ* after incremental addition of freshly prepared L-Trp solution (2.5 × 10^{-3} M). After each addition, the CD spectrum of the suspension was monitored. As demonstrated in Fig. 3a, the intensity of the ICD signal appearing at 325 nm gradually increased with the increase of L-Trp concentration. The linear regression equation was derived from the calibration curve, ICD (mdeg) = 0.13218[C] (μM) − 0.18606 (R^2 = 0.9990), which was established based on the plot of the average value of the ICD signal intensities (325 nm) *versus* L-Trp concentrations in the range from 0 to 4.339 × 10^{-4} M (Fig. 3b). According to the limit of detection (LOD) equation[54] LOD = 3σ/S (σ is the standard deviation of 10 blank measurements, and S is the slope between ICD signal intensity *versus* L-Trp concentration), the LOD was obtained as 2.00 × 10^{-5} M. A good linear relationship provided a chance to efficiently and accurately detect the concentration of L-Trp, as demonstrated by the quantitative detection results of L-Trp concentration discussed below.

Using **LNNU-2** as an ICD sensor, 10 samples with different concentrations of L-Trp aqueous solutions were detected by CD spectroscopy in the range of 7.50 × 10^{-5} to 5.00 × 10^{-4} M, and the intensities of the ICD signals at 325 nm were recorded (Fig. S8 and Table S8†). By substituting the ICD signal intensity into the linear equation ICD (mdeg) = 0.13218[C] (μM) −
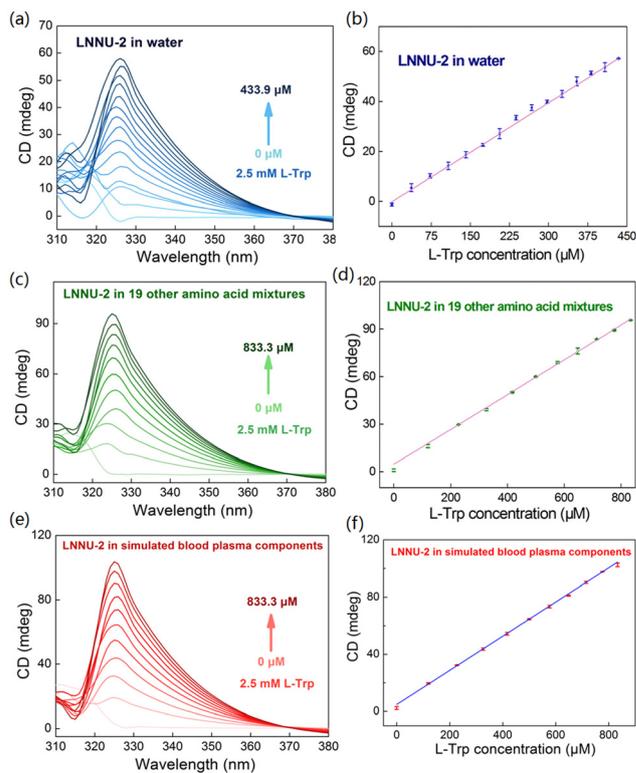
Fig. 3 CD spectra of **LNNU-2** dispersed in water (a), the mixed aqueous solution of 19 other natural amino acids (c) and the simulated blood plasma components (e) upon incremental addition of the L-Trp aqueous solution (2.5 × 10^{-3} M); the linear relationship between ICD intensities at 325 nm and the concentrations of L-Trp in water (b), the mixed aqueous solution of 19 other natural amino acids (d) and the simulated blood plasma components (f).

0.18606, the calculated L-Trp concentration was the detected concentration, which was very close to the actual concentration of the sample. As shown in Table S8,† the actual concentration of the L-Trp sample was 2.78 × 10^{-4} M (entry 6), while the detected concentration was 2.79 × 10^{-4} M. Even for the L-Trp sample with a low concentration, it showed good detection results, that is, the actual concentration in the L-Trp aqueous solution was 7.50 × 10^{-5} M (entry 1), and the detected concentration was 7.83 × 10^{-5} M. The average relative error between the detected and actual concentrations of 10 L-Trp aqueous solution samples was only 2.6%, indicating that **LNNU-2** could accurately and rapidly detect the concentration of L-Trp in water using the CD titration method.

The detection of the concentration of an individual chiral amino acid in a mixture of other chiral amino acids is challenging by using chiral optical sensing techniques due to the similar properties of chiral amino acid molecules. Since **LNNU-2** had high sensitivity for the ICD sensing of L-Trp in water, we tried to determine the concentration of L-Trp in a mixed aqueous solution of 19 other natural amino acids. First, we assessed the selectivity of **LNNU-2** toward natural amino acids. As illustrated in Fig. S9,† the CD spectrum of the **LNNU-2**@L-Trp suspension showed a strong ICD signal at

This journal is © the Partner Organisations 2023

Inorg. Chem. Front., 2023, **10**, 2818–2828 | **2821**

329 nm, while the CD spectra of pure aqueous solutions of all natural amino acids and the suspensions of **LNNU-2**@other natural amino acids exhibited no ICD signals. This result indicated that **LNNU-2** had a high selectivity for the ICD sensing of L-Trp in the presence of other natural amino acids and without interference from the co-existing species. Subsequently, using the same method as the above, a standard curve was established in the L-Trp concentration range from 0 to 8.333×10^{-4} M (Fig. 3c and d), and the linear equation was derived from the standard curve as ICD (mdeg) = 0.1097[C] (μM) + 4.80784 (R^2 = 0.9996). The LOD of L-Trp was calculated to be 2.28×10^{-5} M. The effectiveness of the L-Trp concentration analyses was demonstrated by analyzing 10 L-Trp samples at varying concentrations in the presence of 19 other natural amino acids (Table S8 and Fig. S10†). As shown in Table S8,† the actual concentrations of the L-Trp samples were 2.58×10^{-4} M (entry 1), 3.54×10^{-4} M (entry 3), 5.54×10^{-4} M (entry 8) and 6.82×10^{-4} M (entry 10), and the detected concentrations were 2.54×10^{-4} M, 3.55×10^{-4} M, 5.53×10^{-4} M and 6.80×10^{-4} M, respectively. The average value of the relative error between the detected and actual concentrations of the 10 samples was only 0.7%. The above results indicated that **LNNU-2** could be used as a highly selective ICD sensor for the accurate determination of L-Trp concentration in the presence of other natural amino acids.

Trp is the only amino acid that binds to plasma albumin and exists in a balance between albumin-bound and free forms in the peripheral circulation.[53] Therefore, it is of biological significance to detect the concentration of free L-Trp in blood plasma components. Fortunately, using **LNNU-2** as an ICD sensor, the determination of L-Trp concentration in simulated blood plasma components showed the same accuracy and high selectivity. A standard curve was established using the above same method, and the linear equation ICD (mdeg) = 0.11957[C] (μM) + 4.83409 (R^2 = 0.9996) was obtained (Fig. 3e and f). In addition, the LOD was calculated to be 1.97×10^{-5} M. Based on the measurement and analysis of 10 L-Trp samples at varying concentrations, it was concluded that the **LNNU-2** sensor could also be used to accurately determine the L-Trp concentration in simulated blood plasma components (Table S8 and Fig. S11†). For instance, the actual concentrations of three L-Trp samples were 1.85×10^{-4} M (entry 2), 6.06×10^{-4} M (entry 7) and 8.05×10^{-4} M (entry 10), and the detected concentrations were 1.85×10^{-4} M, 6.07×10^{-4} M and 8.06×10^{-4} M, respectively. The average relative error was only 0.8%. This result indicated that **LNNU-2** could accurately and efficiently determine the concentration of L-Trp in simulated blood plasma components without any interference from other coexisting species.

The recyclability of sensing materials is important for assessing their practicality. Therefore, the recycling performance of **LNNU-2** in water, mixed natural amino acids and simulated blood plasma components was investigated (Fig. S12a–c†). After performing the sensing experiments of **LNNU-2**, the suspensions of **LNNU-2**@L-Trp were centrifuged and washed with water several times, and then the ICD signal of the above sus-

pensions disappeared. Subsequently, an aqueous solution of L-Trp was added to the recycled samples. The results showed that the ICD signals of **LNNU-2**@L-Trp suspensions can be recovered and regenerated. After five continuous cycles, the ICD signal intensities of **LNNU-2**@L-Trp suspensions were basically the same as those of the initial suspensions. Meanwhile, the PXRD patterns of the recycled **LNNU-2** samples revealed that their crystal structure was intact after five cycles (Fig. S12d†). The experimental results indicated that **LNNU-2** has excellent recyclability.

Quantitative enantioselective sensing of chiral Trp

Using the CD titration method, **LNNU-2** achieved the accurate determination of L-Trp concentration at a submillimolar concentration. Compared to **LNNU-1**, **LNNU-2** was expected to serve as an ICD sensor for determining the absolute configuration and ee value of the chiral Trp sample at a lower concentration. As demonstrated in Fig. S13a,† a calibration curve was constructed using samples containing Trp (2.5×10^{-4} M) at varying ee values (+100, +80, +60, +40, +20, 0, −20, −40, −60, −80 and −100%). Notably, a good linear relationship between the average value of the ICD signal intensities (325 nm) and the ee values of Trp samples was observed at submillimolar concentrations. The linear regression equation was calculated from the calibration curve, ICD (mdeg) = 0.32289 ee (%) + 1.8991 (R^2 = 0.9992). Thus, the ICD signal intensity at 325 nm could be used for the determination of the ee values of chiral Trp samples. In addition, the absolute configuration of the sample could be correctly assigned based on the direction of the ICD signal. The validity of the ICD sensing assay was demonstrated by analyzing 10 Trp samples at varying enantiomeric compositions in water (Table 1 and Fig. S13b†). For instance, sensing a mixture containing Trp with an ee value of 96% (entry 1) gave an exact ee value of 95.9%, and it was also able to determine the enantiomeric ratio of the sample at the same time (Table 1). By comparing the reference spectra (Fig. 2b), the absolute configuration of the major enantiomer was determined to be the L configuration. Notably, the absolute configurations of the major enantiomers of the 10 Trp samples were correctly assigned, and the average absolute error between the detected and the actual ee value was only 0.9%.

Quantitative enantioselective sensing of chiral aromatic amino alcohols

The ICD sensing mechanism indicated that if the functional sites of **LNNU-2** highly matched with the active sites of the chiral analyte, multiple noncovalent interactions might be generated between **LNNU-2** and the chiral analyte. Then, the noncovalent interactions might result in the emergence of a strong ICD response, which could achieve the determination of the absolute configuration and ee value of the chiral analyte. Inspired by this work, two chiral aromatic amino alcohols, namely, 2-phenylglycinol (**1**) and (−)-*cis*-1-amino-2-indanol (**2**), were selected for the noncovalent ICD sensing study (Fig. 4a and b).

Table 1 Assignment of the absolute configuration and analysis of the enantiomeric composition of 10 Trp samples (2.5×10^{-4} M) in water

Sample composition				Sensing results			
Entry	Abs. config.	%ee	Ratio L/D	Abs. config.[a]	%ee[b]	Ratio L/D [b]	%ee absolute error
1	L	96.0	98.0 : 2.0	L	95.9	97.9 : 2.1	0.1
2	D	−96.0	2.0 : 98.0	D	−95.5	2.2 : 97.8	0.5
3	L	90.0	95.0 : 5.0	L	88.5	94.3 : 5.7	1.5
4	D	−55.0	22.5 : 77.5	D	−55.1	22.4 : 77.6	0.1
5	L	80.0	90.0 : 10.0	L	81.1	90.6 : 9.4	1.1
6	D	−40.0	30.0 : 70.0	D	−40.9	29.5 : 70.5	0.9
7	L	70.0	85.0 : 15.0	L	68.8	84.4 : 15.6	1.2
8	D	−30.0	35.0 : 65.0	D	−29.0	35.5 : 64.5	1.0
9	L	50.0	75.0 : 25.0	L	50.6	75.3 : 24.7	0.6
10	D	−20.0	40.0 : 60.0	D	−18.5	40.7 : 59.3	1.5

[a] By comparison of the sign of the ICD with the reference spectra (Fig. 2b). [b] Based on ICD signal intensities at 325 nm.
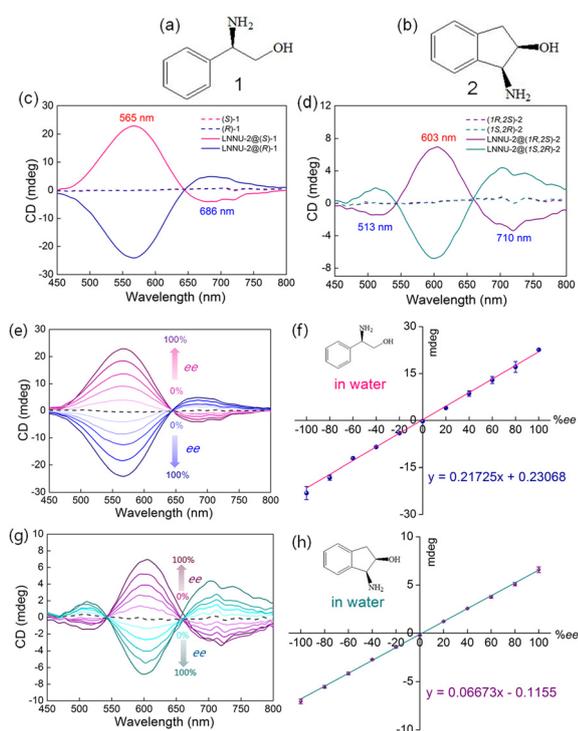
Fig. 4 Molecular structures of (a) 2-phenylglycinol (**1**) and (b) (−)-*cis*-1-amino-2-indanol (**2**); (c) CD spectra of **LNNU-2**@(*S*)-**1**/(*R*)-**1** suspensions and the pure aqueous solutions of (*S*)-**1** and (*R*)-**1**; (d) CD spectra of **LNNU-2**@(**1R,2S**)-**2**/(**1S,2R**)-**2** suspensions and the pure aqueous solutions of (**1R,2S**)-**2** and (**1S,2R**)-**2**; (e) CD spectra of **LNNU-2** interacting with samples of **1** at varying enantiomeric compositions and (f) plot of the ICD signal intensities at 565 nm *versus* ee values of samples of **1** in water; (g) CD spectra of **LNNU-2** interacting with samples of **2** at varying enantiomeric compositions and (h) plot of the ICD signal intensities at 603 nm *versus* ee values of samples of **2** in water.

LNNU-2 (2.0 mg) was dispersed in an aqueous solution (3.0 mL, 3.0×10^{-3} M) of each of the two chiral aromatic amino alcohol enantiomers and sonicated for 20 minutes before CD analysis. As expected, the ICD signals were detected between **LNNU-2** and two chiral aromatic amino alcohols, respectively. The CD spectrum of **LNNU-2**@(*S*)-**1** exhibited a strong positive ICD signal centered at 565 nm and a weak negative ICD signal at 686 nm, while the spectrum of **LNNU-2**@(*R*)-**1** exhibited opposite ICD signals (Fig. 4c). As demonstrated in Fig. 4d, the CD spectrum of **LNNU-2**@(**1R,2S**)-**2** showed a strong positive ICD signal at 603 nm and two weak negative ICD signals at 513 nm and 710 nm, respectively. As expected, the opposite ICD signals were observed in the spectrum of **LNNU-2**@(**1S,2R**)-**2**. Since multiple ICD signals were generated during the ICD sensing process, the strongest ICD signal was selected for the determination of the absolute configuration and ee value of the chiral aromatic amino alcohol sample. Thus, a calibration curve was established based on the plot of the average value of the ICD signal intensities (565 nm) *versus* ee values of samples of **1**, and then the linear regression equation, ICD (mdeg) = 0.21725 ee (%) + 0.23068 (R^2 = 0.9978) (Fig. 4e and f), was derived. Similarly, the linear regression equation ICD (mdeg) = 0.06673 ee (%) − 0.1155 (R^2 = 0.9993) was derived from the calibration curve based on the plot of the average value of the ICD signal intensities (603 nm) *versus* ee values of samples of **2** (Fig. 4g and h).

Based on the good linear relationship, the absolute configuration and ee analyses of the practical sample were further performed simultaneously using the **LNNU-2** sensor. Six samples of **1** and **2** with different enantiomeric compositions were prepared in pure water, respectively. The absolute configuration was determined using the sign of the Cotton effect, and the ICD signal intensities at 565 nm for **1** and 603 nm for **2** were used to quantify ee values. As shown in Table 2 and Fig. S14,† the absolute configurations of the major enantiomers of the above samples could be correctly assigned, and the ee values were also accurately established. The average absolute error between the detected and the actual ee values of the six samples of both **1** and **2** was 1.2%. The results indicated that **LNNU-2** could be used as an ICD sensor for the rapid and accurate quantification of the enantiomeric compositions of two chiral aromatic amino alcohols in water without the involvement of any organic solvent.

This journal is © the Partner Organisations 2023

Inorg. Chem. Front., 2023, **10**, 2818–2828 | **2823**

Table 2 Assignment of the absolute configuration and analysis of the enantiomeric composition of 2-phenylglycinol (**1**) and (−)-*cis*-1-amino-2-indanol (**2**) samples in pure water

Sample 1 composition				Sensing results			
Entry	Abs. config.	%ee	Ratio *R*/*S*	Abs. config.[a]	%ee[b]	Ratio *R*/*S*[b]	%ee absolute error
1	*R*	−88.0	94.0 : 6.0	*R*	−88.9	94.5 : 5.5	0.9
2	*S*	85.0	7.5 : 92.5	*S*	83.6	8.2 : 91.8	1.4
3	*R*	−48.0	74.0 : 26.0	*R*	−47.4	73.7 : 26.3	0.6
4	*S*	60.0	20.0 : 80.0	*S*	61.7	19.1 : 80.9	1.7
5	*R*	−32.0	66.0 : 34.0	*R*	−32.9	66.5 : 33.5	0.9
6	*S*	48.0	26.0 : 74.0	*S*	46.2	26.9 : 73.1	1.8

| Sample 2 composition				Sensing results			
Entry	Abs. config.	%ee	Ratio 1*R*,2*S*/1*S*,2*R*	Abs. config.[a]	%ee[b]	Ratio 1*R*,2*S*/1*S*,2*R*[b]	%ee absolute error
1	1*R*,2*S*	90.0	95.0 : 5.0	1*R*,2*S*	88.2	94.1 : 5.9	1.8
2	1*S*,2*R*	−92.0	4.0 : 96.0	1*S*,2*R*	−91.5	4.2 : 95.8	0.5
3	1*R*,2*S*	49.0	74.5 : 25.5	1*R*,2*S*	47.4	73.7 : 26.3	1.6
4	1*S*,2*R*	−66.0	17.0 : 83.0	1*S*,2*R*	−64.7	17.6 : 82.4	1.3
5	1*R*,2*S*	28.0	64.0 : 36.0	1*R*,2*S*	27.4	63.7 : 36.3	0.6
6	1*S*,2*R*	−40.0	30.0 : 70.0	1*S*,2*R*	−38.4	30.8 : 69.2	1.6

[a] By comparison of the sign of the ICD with the reference spectra (Fig. 4c and d). [b] Based on ICD signal intensities at 565 nm for **1** and 603 nm for **2**.

Chiral induction synthesis of enantioenriched LNNU-2

Single-crystal structural analysis revealed that **LNNU-2** crystallized in a chiral space group of $P2_12_12_1$ with a Flack absolute configuration parameter of 0.029(4), indicating the enantiomeric purity of the single crystal (Table S1†).[55] Although the phosphonic acid ligand (H_2L) had a chiral phosphorus (P) center, the raw material used to synthesize H_2L was achiral, resulting in H_2L becoming a racemate. Therefore, the chirality of bulk samples of **LNNU-2** should be random. To determine the chiral purity of **LNNU-2**, 20 single-crystal samples were randomly picked from the same batch and their solid-state CD spectra were recorded. Each single-crystal sample was found to be CD active, and 13 of them were in the *M*-configuration and 7 in the *P*-configuration (Fig. S15†). Apparently, two enantiomers (*M* and *P*) were present in the bulk **LNNU-2** samples with a slight excess of the *M*-configuration.

Although many chiral MOFs with novel structures and excellent properties have been successfully obtained, the synthesis of homochiral or enantioenriched MOFs remains a challenge.

Chiral induction is an effective method for the synthesis of homochiral or enantioenriched MOFs, and the appropriate interactions between chiral inducers and achiral building blocks are very important for chiral induction synthesis.[56] Inspired by the results of the noncovalent ICD sensing mechanism, chiral Trp could be a candidate for chiral induction due to the existence of multiple noncovalent interactions between **LNNU-2** and chiral Trp. Therefore, we attempted to split two enantiomers of **LNNU-2** to obtain enantioenriched (*P*)-**LNNU-2** and (*M*)-**LNNU-2** using L-Trp and D-Trp as chiral inducers, respectively. The synthesis of enantioenriched **LNNU-2** was carried out by replacing deionized water with an aqueous solu-
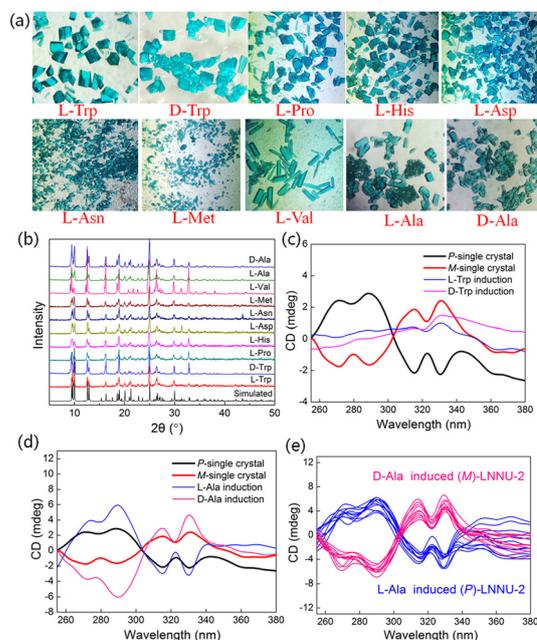
Fig. 5 (a) Images and (b) PXRD patterns of **LNNU-2** products induced by chiral amino acids; (c) solid-state CD spectra of **LNNU-2** products induced by L-Trp and D-Trp; (d) solid-state CD spectra of **LNNU-2** products induced by L-Ala and D-Ala; (e) solid-state CD spectra of 10 randomly selected samples induced by L-Ala/D-Ala from the same batch.

tion of L-Trp (or D-Trp) at a concentration of 2.5×10^{-3} M, while the other original synthesis conditions of **LNNU-2** remained unchanged. As a result, blue block crystals were obtained, and the PXRD patterns of products showed that they had the same framework structure as **LNNU-2** (Fig. 5a and b).

However, solid-state CD spectra of the products showed that they had no CD activity either induced with L-Trp or D-Trp (Fig. 5c). This result indicated that the strong noncovalent interactions between **LNNU-2** and chiral Trp were not favorable for the synthesis of enantioenriched **LNNU-2**. Therefore, using the same synthesis method, other different types of chiral amino acids were selected as chiral inducers for the chiral induction synthesis of **LNNU-2** (Table S9†).

As shown in Fig. 5a, the **LNNU-2** products induced by chiral amino acids were all blue block crystals, and the PXRD patterns of products confirmed that their framework structures were the same as that of **LNNU-2** (Fig. 5b). Solid-state CD spectra showed that **LNNU-2** bulk samples induced by L-proline (L-Pro), L-histidine (L-His) and L-aspartate (L-Asn) had Cotton effects similar to that of the single-crystal sample of (*M*)-**LNNU-2** (Fig. S16a†). The only difference was that all CD spectra of these products had an additional positive CD signal near 260 nm. This suggested that the above products might not be enantioenriched but enantiomeric excess (*M* > *P*). In contrast, when L-aspartic acid (L-Asp), L-methionine (L-Met) and L-valine (L-Val) were selected as chiral inducers, the solid-state CD spectra of bulk samples of the products showed no CD activity, indicating that they were all racemates (Fig. S16b†). Surprisingly, the solid-state CD spectra of the products inducted by L-Ala exhibited a Cotton effect opposite to that of the single-crystal sample of (*M*)-**LNNU-2**, suggesting the successful synthesis of (*P*)-**LNNU-2** samples (Fig. 5d). Meanwhile, single-crystal structural analysis of the products revealed the presence of *P*-helical chains in the crystal structure, which had mirror symmetry with the *M*-configuration (Fig. S17†). A Flack parameter of 0.025(4) further verified that the *P*-configuration was determined correctly (Table S10†).[55] To determine the chiral purity of bulk samples of the products induced by L-Ala, the solid-state CD spectra of 10 bulk samples randomly picked from the same batch were measured (Fig. 5e). The results showed the same Cotton effects as that of the single-crystal sample of (*P*)-**LNNU-2**. The above results indicated that the enantioenriched (*P*)-**LNNU-2** samples were successfully synthesized using L-Ala as a chiral inducer. Similarly, the enantioenriched (*M*)-**LNNU-2** samples were also successfully obtained upon chiral induction of D-Ala. The solid-state CD spectra of 10 bulk samples randomly picked from the same batch had the same Cotton effect as that of the single-crystal sample with the *M*-configuration (Fig. 5e). Furthermore, two parallel syntheses of **LNNU-2** were carried out using L-Ala and D-Ala as the chiral inducers, respectively. The solid-state CD spectra of 5 bulk samples randomly picked from each synthesis were the same as before (Fig. S18†). The results of crystal structure analyses and solid-state CD spectra demonstrated that two enantiomers of **LNNU-2**, (*P*)-[Cu(L)(2,2′-bipy)]·H$_2$O ((*P*)-**LNNU-2**) and (*M*)-[Cu(L)(2,2′-bipy)]·H$_2$O ((*M*)-**LNNU-2**), were successfully obtained by chiral induction, and L-Ala and D-Ala were suitable chiral inducers for the synthesis of enantioenriched **LNNU-2** samples.

The above results suggested that using different chiral amino acids as chiral inducers resulted in products with the same framework structure but different chiral features. Apparently, different amino acid inducers have different chiral induction effects on the synthesis of **LNNU-2**. It was found that the strong noncovalent interactions between **LNNU-2** and chiral Trp reduced the degree of enantiomeric excess of **LNNU-2**, and the products changed from a slight enantiomeric excess to racemic. This suggested that too strong interactions between chiral inducers and building blocks were not conducive to the formation of enantioenriched products. Among the different types of chiral amino acids used as chiral inducers, only chiral Ala induced the enantioenriched **LNNU-2**. Compared with other chiral amino acids, chiral Ala is the simplest chiral amino acid in terms of the molecular structure and low positional resistance (Table S9†). Compared with chiral Trp, the molecular structure of chiral Ala lacked an aromatic group, so there was no π···π interaction between chiral Ala and **LNNU-2**. This weakened the degree of noncovalent interactions between the chiral inducer and the building blocks of **LNNU-2**. Instead, it is more favorable to generate the enantioenriched **LNNU-2** in chiral induction synthesis. It could be seen that the rational control of the degree of noncovalent interactions between chiral inducers and framework building blocks might have a significant effect on the generation of enantioenriched products. Although we could not explain exactly why the enantioenriched **LNNU-2** was successfully obtained upon chiral induction of L-Ala and D-Ala, the above-mentioned studies could provide ideas for screening suitable chiral inducers for the synthesis or splitting of chiral MOFs.

Conclusions

In summary, two new chiral MOFs, namely [Cu(L)(2,2′-bipy)]·H$_2$O (**LNNU-2**) and [Cd(L)(2,2′-bipy)(H$_2$O)] (**LNNU-3**), and a series of bimetallic MOFs, [Zn$_x$Cu$_y$(L)(2,2′-bipy)]·H$_2$O ($x : y$ = 9.6 : 0.4–1.0 : 9.0), were successfully designed and synthesized for the study of the noncovalent ICD sensing mechanism. By observing the differences in ICD signals between the above MOFs and L-Trp or between **LNNU-2** and L-Trp and its derivatives, the effects of noncovalent interactions on the generation and amplification of ICD signals were investigated. The results indicated that multiple noncovalent interactions facilitated the output and amplification of the ICD signal. In this ICD sensing system, the metal coordination interaction played a decisive role in the generation of ICD signals, while the hydrogen bonding interaction only affected the amplification degree of the ICD signal. The strength of the ICD signal increased with the enhancement of the Lewis acidity of the metal center of the MOFs. Thus, **LNNU-2** showed improved ICD sensing performance compared to the previously reported **LNNU-1** sensor. **LNNU-2** allowed the quantification of the enantiomeric composition of the chiral Trp sample at a lower concentration. More importantly, the amplified ICD signal of the **LNNU-2**@L-Trp suspension enabled highly selective and accurate determination of L-Trp concentration in water, mixed natural amino

This journal is © the Partner Organisations 2023

Inorg. Chem. Front., 2023, **10**, 2818–2828 | **2825**

acids and simulated blood plasma components, respectively. Based on the noncovalent ICD sensing mechanism, **LNNU-2** also achieved rapid and accurate determination of the absolute configuration and ee values of the chiral aromatic amino alcohols in pure water. In addition, different chiral amino acids were selected as chiral inducers for the chiral induction synthesis of enantioenriched **LNNU-2**. Remarkably, **LNNU-2** was successfully split into enantioenriched (**P**)-**LNNU-2** and (**M**)-**LNNU-2** upon chiral induction of ʟ-Ala and ᴅ-Ala. This work provides new ideas for the rational design of MOF-based noncovalent ICD sensors and the screening of suitable chiral inducers for chiral induction synthesis.

Author contributions

Z. S. and C. J. conceived the concept and directed the project. Y. Z. designed the study, conducted most of the experiments, wrote the original draft and revised the manuscript. T. D. performed the experiments. X. Z., Y. Z., J. Y. and X. L. collected and analyzed the data. H. Z., C. J. and Z. S. modified the manuscript.

Conflicts of interest

There are no conflicts to declare.

Acknowledgements

References

1 G. Pályi, *Biological Chirality*, *Elsevier*, London, 2019.

2 V. Davankov, Chirality as an Inherent General Property of Matter, *Chirality*, 2006, **18**, 459–461.

3 D. P. Glavin, A. S. Burton, J. E. Elsila, J. C. Aponte and J. P. Dworkin, The Search for Chiral Asymmetry as a Potential Biosignature in our Solar System, *Chem. Rev.*, 2020, **120**, 4660–4689.

4 P. Peluso and B. Chankvetadze, Recognition in the Domain of Molecular Chirality: From Noncovalent Interactions to Separation of Enantiomers, *Chem. Rev.*, 2022, **122**, 13235–13400.

5 F. Pop, N. Zigon and N. Avarvari, Main-Group-Based Electro- and Photoactive Chiral Materials, *Chem. Rev.*, 2019, **119**, 8435–8478.

6 J. Liu, S. Mukherjee, F. Wang, R. A. Fischer and J. Zhang, Homochiral Metal-Organic Frameworks for Enantioseparation, *Chem. Soc. Rev.*, 2021, **50**, 5706–5745.

7 A. Gheorghe, M. A. Tepaske and S. Tanase, Homochiral Metal-Organic Frameworks as Heterogeneous Catalysts, *Inorg. Chem. Front.*, 2018, **5**, 1512–1523.

8 I. D. Rukhlenko, N. V. Tepliakov, A. S. Baimuratov, S. A. Andronaki, Y. K. Guńko, A. V. Baranov and A. V. Fedorov, Completely Chiral Optical Force for Enantioseparation, *Sci. Rep.*, 2016, **6**, 36884.

9 A. Gogoi, N. Mazumder, S. Konwer, H. Ranawat, N.-T. Chen and G.-Y. Zhuo, Enantiomeric Recognition and Separation by Chiral Nanoparticles, *Molecules*, 2019, **24**, 1007.

10 D. C. Patel, M. F. Wahab, D. W. Armstrong and Z. S. Breitbach, Advances in High-Throughput and High-Efficiency Chiral Liquid Chromatographic Separations, *J. Chromatogr. A*, 2016, **1467**, 2–18.

11 I. Ilisz, A. Péter and W. Lindner, State-of-the-Art Enantioseparations of Natural and Unnatural Amino Acids by High-Performance Liquid Chromatography, *Trends Anal. Chem.*, 2016, **81**, 11–22.

12 V. Schurig, Practice and Theory of Enantioselective Complexation Gas Chromatography, *J. Chromatogr. A*, 2002, **965**, 315–356.

13 L. Yang, T. Wenzel, R. T. Williamson, M. Christensen, W. Schafer and C. J. Welch, Expedited Selection of NMR Chiral Solvating Agents for Determination of Enantiopurity, *ACS Cent. Sci.*, 2016, **2**, 332–340.

14 Y. Zhao and T. M. Swager, Simultaneous Chirality Sensing of Multiple Amines by ^{19}F NMR, *J. Am. Chem. Soc.*, 2015, **137**, 3221–3224.

15 G. Storch, M. Haas and O. Trapp, Attracting Enantiomers: Chiral Analytes that are Simultaneously Shift Reagents Allow Rapid Screening of Enantiomeric Ratios by NMR Spectroscopy, *Chem. – Eur. J.*, 2017, **23**, 5414–5418.

16 Z. Chen, Q. Wang, X. Wu, Z. Li and Y.-B. Jiang, Optical Chirality Sensing Using Macrocycles, Synthetic and Supramolecular Oligomers/Polymers, and Nanoparticle Based Sensors, *Chem. Soc. Rev.*, 2015, **44**, 4249–4263.

17 S. Thoonen and C. Hua, Chiral Detection with Coordination Polymers, *Chem. – Asian J.*, 2021, **16**, 890–901.

18 L. Pu, Enantioselective Fluorescent Recognition of Free Amino Acids: Challenges and Opportunities, *Angew. Chem., Int. Ed.*, 2020, **59**, 21814–21828.

19 W. Ma, L. Xu, L. Wang, C. Xu and H. Kuang, Chirality-Based Biosensors, *Adv. Funct. Mater.*, 2019, **29**, 1805512.

20 X. Zhang, J. Yin and J. Yoon, Recent Advances in Development of Chiral Fluorescent and Colorimetric Sensors, *Chem. Rev.*, 2014, **114**, 4918–4959.

21 Z. A. De los Santos, C. C. Lynch and C. Wolf, Optical Chirality Sensing with an Auxiliary-free Earth-abundant Cobalt Probe, *Angew. Chem., Int. Ed.*, 2019, **58**, 1198–1202.

22 D. Wu, Y. Yu, J. Zhang, L. Guo and Y. Kong, Chiral Poly (ionic liquid) with Nonconjugated Backbone as a Fluorescent Enantioselective Sensor for Phenylalaninol and

Tryptophan, *ACS Appl. Mater. Interfaces*, 2018, **10**, 23362–23368.

23 Z.-Z. Weng, H. Xu, W. Zhang, G.-L. Zhuang, L.-S. Long, X.-J. Kong and L.-S. Zheng, Enantioselective Recognition and Separation of *C*₂ Symmetric Substances via Chiral Metal-Organic Frameworks, *ACS Appl. Mater. Interfaces*, 2021, **13**, 37412–37421.

24 B. Li, J. Zhang, L. Li and G. Chen, Rapid and Sensitive Method for Chiroptical Sensing of *α*-Amino Acids *via* Click-Like Labeling with *o*-Phthalaldehyde and *p*-Toluenethiol, *Chem. Sci.*, 2021, **12**, 2504–2508.

25 L. Pu, Chemoselective and Enantioselective Fluorescent Identification of Specific Amino Acid Enantiomers, *Chem. Commun.*, 2022, **58**, 8038–8048.

26 Z. Sharifzadeh, K. Berijani and A. Morsali, Chiral Metal-Organic Frameworks Based on Asymmetric Synthetic Strategies and Applications, *Coord. Chem. Rev.*, 2021, **445**, 214083.

27 M. M. Wanderley, C. Wang, C.-D. Wu and W. Lin, A Chiral Porous Metal-Organic Framework for Highly Sensitive and Enantioselective Fluorescence Sensing of Amino Alcohols, *J. Am. Chem. Soc.*, 2012, **134**, 9050–9053.

28 T.-Y. Liu, X.-L. Qu and B. Yan, A Sensitive Metal-Organic Framework Nanosensor with Cation-Introduced Chirality for Enantioselective Recognition and Determination of Quinine and Quinidine in Human Urine, *J. Mater. Chem. C*, 2020, **8**, 14579–14586.

29 P. Chandrasekhar, A. Mukhopadhyay, G. Savitha and J. N. Moorthy, Remarkably Selective and Enantiodifferentiating Sensing of Histidine by a Fluorescent Homochiral Zn–MOF Based on Pyrene-Tetralactic Acid, *Chem. Sci.*, 2016, **7**, 3085–3091.

30 Q. Zhang, M. Lei, F. Kong and Y. Yang, A Water-Stable Homochiral Luminescent MOF Constructed from an Achiral Acylamide-Containing Dicarboxylate Ligand for Enantioselective Sensing of Penicillamine, *Chem. Commun.*, 2018, **54**, 10901–10904.

31 Z. Han, K. Wang, Y. Guo, W. Chen, J. Zhang, X. Zhang, G. Siligardi, S. Yang, Z. Zhou, P. Sun, W. Shi and P. Cheng, Cation-Induced Chirality in a Bifunctional Metal-Organic Framework for Quantitative Enantioselective Recognition, *Nat. Commun.*, 2019, **10**, 5117.

32 S. Li, Y. Zhou and B. Yan, Zirconium Metal Organic Framework-Based Hybrid Sensors with Chiral and Luminescent Centers Fabricated by Postsynthetic Modification for the Detection and Recognition of Tryptophan Enantiomers, *Inorg. Chem.*, 2022, **61**, 9615–9622.

33 Y. W. Zhao, Y. Wang and X. M. Zhang, Homochiral MOF as Circular Dichroism Sensor for Enantioselective Recognition on Nature and Chirality of Unmodified Amino Acids, *ACS Appl. Mater. Interfaces*, 2017, **9**, 20991–20999.

34 R. X. Yao, H. H. Fu, B. Yu and X. M. Zhang, Chiral Metal-Organic Frameworks Constructed from Four-fold Helical Chain SBUs for Enantioselective Recognition of α-Hydroxy/Amino Acids, *Inorg. Chem. Front.*, 2018, **5**, 153–159.

35 C.-X. Tan, K.-W. Yang, J.-Q. Dong, Y.-H. Liu, Y. Liu, J.-W. Jiang and Y. Cui, Boosting Enantioselectivity of Chiral Organocatalysts with Ultrathin Two-Dimensional Metal-Organic Framework Nanosheets, *J. Am. Chem. Soc.*, 2019, **141**, 17685–17695.

36 Y.-W. Zhao and X.-M. Zhang, The Construction of Helicate Metal–Organic Nanotubes and Enantioselective Recognition, *J. Mater. Chem. C*, 2020, **8**, 4453–4460.

37 Y.-H. Han, Y.-C. Liu, X.-S. Xing, C.-B. Tian, P. Lin and S.-W. Du, Chiral Template Induced Homochiral MOFs Built from Achiral Components: SHG Enhancement and Enantioselective Sensing of Chiral Alkamines by Ion Exchange, *Chem. Commun.*, 2015, **51**, 14481–14484.

38 Y.-W. Zhao, L.-E. Guo, F.-Q. Zhang, J. Yao and X.-M. Zhang, Turn-On Fluorescence Enantioselective Sensing of Hydroxyl Carboxylic Enantiomers by Metal–Organic Framework Nanosheets with a Homochiral Tetracarboxylate of Cyclohexane Diamide, *ACS Appl. Mater. Interfaces*, 2021, **13**, 20821–20829.

39 X. Zhao, E. T. Nguyen, A. N. Hong, P. Feng and X. Bu, Chiral Isocamphoric Acid: Founding a Large Family of Homochiral Porous Materials, *Angew. Chem., Int. Ed.*, 2018, **57**, 7101–7105.

40 S. Allenmark, Induced Circular Dichroism by Chiral Molecular Interaction, *Chirality*, 2003, **15**, 409–422.

41 M. Quan, X.-Y. Pang and W. Jiang, Circular Dichroism Based Chirality Sensing with Supramolecular Host–Guest Chemistry, *Angew. Chem., Int. Ed.*, 2022, **61**, e202201258.

42 H. Fenniri, B. L. Deng and A. E. Ribbe, Helical Rosette Nanotubes with Tunable Chiroptical Properties, *J. Am. Chem. Soc.*, 2002, **124**, 11064–11072.

43 K. W. Bentley and C. Wolf, Stereodynamic Chemosensor with Selective Circular Dichroism and Fluorescence Readout for in Situ Determination of Absolute Configuration, Enantiomeric Excess, and Concentration of Chiral Compounds, *J. Am. Chem. Soc.*, 2013, **135**, 12200–12203.

44 F. Biedermann and W. M. Nau, Noncovalent Chirality Sensing Ensembles for the Detection and Reaction Monitoring of Amino Acids, Peptides, Proteins, and Aromatic Drugs, *Angew. Chem., Int. Ed.*, 2014, **53**, 5694–5699.

45 M. Hasan, V. N. Khose, A. D. Pandey, V. Borovkov and A. V. Karnik, Tailor-Made Supramolecular Chirogenic System Based on *C*ₛ-Symmetric Rigid Organophosphoric Acid Host and Amino Alcohols: Mechanistic Studies, Bulkiness Effect, and Chirality Sensing, *Org. Lett.*, 2016, **18**, 440–443.

46 S. L. Pilicer, P. R. Bakhshi, K. W. Bentley and C. Wolf, Biomimetic Chirality Sensing with Pyridoxal-5′-phosphate, *J. Am. Chem. Soc.*, 2017, **139**, 1758–1761.

47 W. Zuo, Z. Huang, Y. Zhao, W. Xu, Z. Liu, X.-J. Yang, C. Jia and B. Wu, Chirality Sensing of Choline Derivatives by a Triple Anion Helicate Cage through Induced Circular Dichroism, *Chem. Commun.*, 2018, **54**, 7378–7381.

This journal is © the Partner Organisations 2023

Inorg. Chem. Front., 2023, **10**, 2818–2828 | **2827**

48 K. Liu, G. Du, L. Ye and L. Jiang, Chiroptical Nanoprobe for Highly Selective Recognition of Histidine Enantiomers in Aqueous Media, *Sens. Actuators, B*, 2019, **284**, 55–62.

49 E. Nelson, J. S. S. K. Formen and C. Wolf, Rapid Organocatalytic Chirality Analysis of Amines, Amino Acids, Alcohols, Amino Alcohols and Diols with Achiral Iso(thio)cyanate Probes, *Chem. Sci.*, 2021, **12**, 8784–8790.

50 Z. A. De los Santos, S. MacAvaney, K. Russell and C. Wolf, Tandem Use of Optical Sensing and Machine Learning for the Determination of Absolute Configuration, Enantiomeric and Diastereomeric Ratios, and Concentration of Chiral Samples, *Angew. Chem., Int. Ed.*, 2020, **59**, 2440–2448.

51 Y.-Y. Zhu, Y.-N. Zhou, X. Zhang, Z.-G. Sun and C.-Q. Jiao, Homochiral MOF as Chiroptical Sensor for Determination of Absolute Configuration and Enantiomeric Ratio of Chiral Tryptophan, *Adv. Opt. Mater.*, 2021, **9**, 2001889.

52 Y. Zhou and J. Yoon, Recent Progress in Fluorescent and Colorimetric Chemosensors for Detection of Amino Acids, *Chem. Soc. Rev.*, 2012, **41**, 52–67.

53 J. P. Ruddick, A. K. Evans, D. J. Nutt, S. L. Lightman, G. A. W. Rook and C. A. Lowry, Tryptophan Metabolism in the Central Nervous System: Medical Implications, *Expert Rev. Mol. Med.*, 2006, **8**, 1–27.

54 Analytical Methods Committee, Recommendations for the Definition, Estimation and Use of the Detection Limit, *Analyst*, 1987, **112**, 199–204.

55 H. D. Flack and G. Bernardinelli, The Use of X-ray Crystallography to Determine Absolute Configuration, *Chirality*, 2008, **20**, 681–690.

56 R. E. Morris and X. Bu, Induction of Chiral Porous Solids Containing only Achiral Building Blocks, *Nat. Chem.*, 2010, **2**, 353–361.